Chapter 18
Delamination Buckling in Composite Plates: an Analytical Approach to Predict Delamination Growth

Anton Köllner, Fabian Forsbach & Christina Völlmecke

Abstract An analytical modelling approach is presented which is capable of determining the post-buckling responses as well as the onset of delamination growth of multi-layered composite plates with an embedded circular delamination. In order to overcome current drawbacks of analytical models regarding embedded delaminations, the model employs a problem description in cylindrical coordinates and a novel geometric representation of delamination growth in conjunction with a Rayleigh-Ritz formulation and the so-called crack-tip element analysis. The modelling approach is applied to study the compressive response of composite plates with thin-film delaminations loaded under radial compressive strain. Post-buckling responses and the onset of delamination growth are determined for several layups. The results are in very good agreement with finite element simulations while requiring low computational cost.

Keywords: Delamination buckling · Energy release rate · Composites · Plates · Delamination

18.1 Introduction

Delamination buckling is a well-known failure mode in layered slender structures which has attracted a lot of interest since the pioneering work of Kachanov (Kachanov, 1976) and Chai et al. (Chai and Babcock, 1985; Chai et al, 1981). Owing to its relevance, particularly for the aircraft industry (Baker and Murray, 2016; Butler et al, 2012), the problem of delaminated composite structures loaded un-

Anton Köllner · Fabian Forsbach · Christina Völlmecke
Technische Universität Berlin, Institute of Mechanics, Stability and Failure of Functionally Optimized Structures Group, Einsteinufer 5, 10587 Berlin, Germany,
e-mail: anton.koellner@tu-berlin.de, fabianfo@mailbox.tu-berlin.de,
christina.voellmecke@tu-berlin.de

B. E. Abali et al. (eds.), *New Achievements in Continuum Mechanics and Thermodynamics*, Advanced Structured Materials 108,
https://doi.org/10.1007/978-3-030-13307-8_18

der in-plane compression represents an area of ongoing research (Chen et al, 2018; Köllner and Völlmecke, 2018; Ouyang et al, 2018). Significant progress has recently been made regarding analytical modelling approaches (Köllner et al, 2018; Köllner and Völlmecke, 2017a,b, 2018) providing insight into the interaction of stability and material failure by determining the post-buckling behaviour during delamination growth and investigating the effect of damage types, dimensions and locations. The effect of delamination location (Ipek et al, 2018; Nilsson et al, 2001), layups (i.e. anisotropy of the sublaminates Butler et al, 2012), local-global buckling (Rhead et al, 2017) and stiffeners (Ouyang et al, 2018) has also been investigated in experimental studies. On the other hand, current numerical studies (Abir et al, 2017; Sun and Hallet, 2018; Tan et al, 2016) mainly investigate the compressive response of certain configurations of damaged composite panels, where damage originated from out-of-plane impact scenarios.

Regarding the evaluation of the compressive strength of delaminated composite panels, the accurate prediction of the onset of delamination growth is important. Analytical models considering embedded delaminations are hitherto not capable of determining the energy release rate along the boundary, which is required to determine the onset of delamination growth precisely. Therefore, the current work aims at improving the capabilities of analytical modelling approaches further by resolving one of the major drawbacks regarding the application of analytical descriptions to embedded delaminations: the prediction of delamination growth by an increase in the initial radius (circular delaminations) (Bottega and Maewal, 1983) or in the major and minor axis (elliptical delaminations), which is commonly referred to as *global* approach.

However, except for certain configurations of the initial delamination (cf. Köllner and Völlmecke, 2018), the global description does not allow for an accurate prediction of the onset of delamination growth (applied load, displacement field, shape of growth) or requires simple model reductions such that only the load causing growth can be approximated (Butler et al, 2012). The current modelling approach considers delamination growth along the boundary of the delamination, thus delamination growth is not associated with a complete disbond of the boundary, which is referred to as *local* approach. This is enabled by using cylindrical coordinates (r, φ, z) as well as a geometric representation of the newly generated delamination area. Despite the resulting dependence of the stiffness tensor on the angle φ, the total potential energy, the equilibrium equations and the energy release rate can be determined analytically yielding an efficient engineering tool to adequately predict post-buckling responses and the onset of delamination growth in multi-layered composite panels with embedded delaminations.

18.2 Model Description

The geometric model and the geometric representation of delamination growth are shown in Fig. 18.1. The circular plate has a radius R^* and a thickness t. The depth of

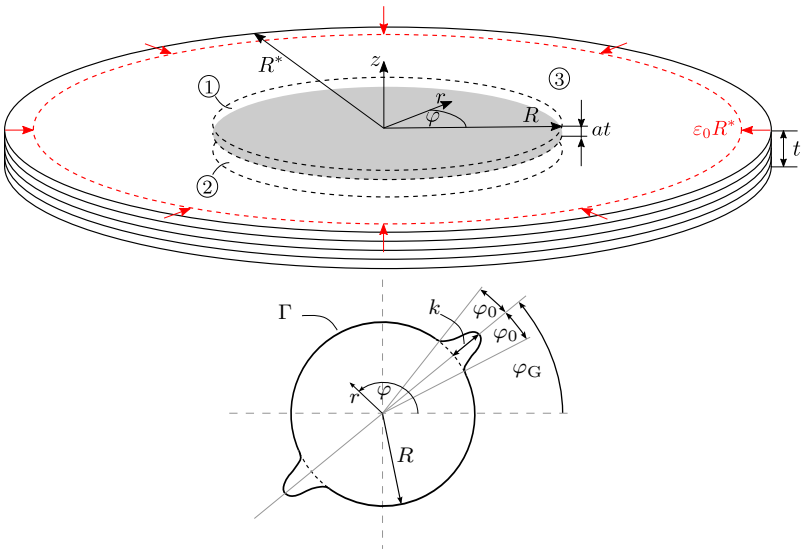

Fig. 18.1 Geometric model of the delaminated plate (top), visualization of the geometric representation of local growth (bottom).

the delamination is defined by the parameter a. Since, in the current work, thin-film delaminations are studied, delaminations complying with $a < 0.1$ are considered. The initial radius of the circular delamination is denoted by R. The plate is subjected to an compressive in-plane radial strain ε_0.

The plate is subdivided into three parts. Parts ① and ② describe the upper and lower sublaminate respectively; part ③ represents the intact region of the plate. It is further assumed that $R^* \gg R$, such that, owing to the thin-film assumption, only the upper delaminated region ① undergoes buckling (out-of-plane deflections).

Delamination growth is modelled with the aid of a trigonometric function added to the given initial radius R in the region where delamination growth is present. Therefore, three parameters φ_G, k and φ_0 are introduced representing the direction of delamination growth, the amplitude of the newly generated delamination and the span of growth respectively. Thus, the boundary of the delamination Γ can be defined as

$$\Gamma = \begin{cases} R + k\cos^2\left(\frac{\varphi-\varphi_G}{\varphi_0}\frac{\pi}{2}\right) & \text{for } \varphi_G - \varphi_0 \le \varphi \le \varphi_G + \varphi_0 \\ R, \quad \text{elsewhere} \end{cases}, \tag{18.1}$$

where, owing to the symmetry of the problem, half of the plate can be considered, i.e. $0 \le \varphi \le \pi$. The trigonometric description used is in good agreement with experimental observations made regarding embedded circular delaminations (cf. Nilsson et al (2001)).

The Classical Laminate Theory (Reddy, 2004) is employed since out-of-plane shear effects are deemed small for the laminates considered (the thin-film assumption). The post-buckling behaviour is modelled with the aid of a RAYLEIGH–RITZ formulation where the displacement field is approximated using a set of generalized coordinates q_i. However, as aforementioned, parts ② and ③ experience no out-of-plane displacement, such that their displacement field $\boldsymbol{u}^{\textcircled{i}}$ can be defined as

$$\begin{aligned} u^{\textcircled{i}}(r,\varphi) &= \varepsilon_0 r, \\ v^{\textcircled{i}}(r,\varphi) &= 0, \\ w^{\textcircled{i}}(r,\varphi) &= 0, \end{aligned} \tag{18.2}$$

where u, v and w are the radial, circumferential and out-of-plane displacements respectively, ε_0 is the loading parameter and $i = 2, 3$. The displacement field of the upper sublaminate is approximated by employing a series of axisymmetric and non-axisymmetric continuous shape functions, thus

$$\begin{aligned} u^{\textcircled{1}}(r,\varphi) &= \varepsilon_0 r + \sum_{m=1}^{M^u}\sum_{n=0}^{N^u} \sin\left(m\pi\frac{r}{\Gamma}\right)\left(a^u_{mn}\sin(2n\varphi) + b^u_{mn}\cos(2n\varphi)\right), \\ v^{\textcircled{1}}(r,\varphi) &= \sum_{m=1}^{M^v}\sum_{n=1}^{N^v} \sin(m\pi\frac{r}{\Gamma})\left(a^v_{mn}\sin(2n\varphi) + b^v_{mn}\cos(2n\varphi)\right), \\ w^{\textcircled{1}}(r,\varphi) &= \sum_{m=1}^{M_1^w} c^w_m\left(\cos\left(m\pi\frac{r}{\Gamma}\right) + (-1)^{m+1}\right) \\ &\quad + \sum_{m=1}^{M_2^w}\sum_{n=1}^{N^w}\sum_{o=1}^{O^w} \sin\left(m\pi\frac{r}{\Gamma}\right)\sin\left(n\pi\frac{r}{\Gamma}\right)\left(a^w_{mno}\sin(2o\varphi)\right. \\ &\quad \left. + b^w_{mno}\cos(2o\varphi)\right), \end{aligned} \tag{18.3}$$

where a^u_{mn}, b^u_{mn}, a^v_{mn}, b^v_{mn}, c^w_m, a^w_{mno} and b^w_{mno} are sets of generalized coordinates which will subsequently be summarized in the set q_i. Eqs. (18.2) and (18.3) comply with the geometric boundary conditions:

$$\begin{aligned} u^{\textcircled{i}}(r=\Gamma,\varphi) &= u^{\textcircled{1}}(r=\Gamma,\varphi) &&= \varepsilon_0\Gamma, \\ v^{\textcircled{i}}(r=\Gamma,\varphi) &= v^{\textcircled{1}}(r=\Gamma,\varphi) &&= 0, \\ w^{\textcircled{i}}(r=\Gamma,\varphi) &= w^{\textcircled{1}}(r=\Gamma,\varphi) &&= 0, \\ \nabla_j w^{\textcircled{i}}(r=\Gamma,\varphi) &= \nabla_j w^{\textcircled{1}}(r=\Gamma,\varphi) &&= 0, \end{aligned} \tag{18.4}$$

with $\nabla_j = \{\frac{\partial}{\partial r}, \frac{1}{r}\frac{\partial}{\partial\varphi}\}$ and $i = 2, 3$.

The amount of generalized coordinates required to adequately model the post-buckling responses varies strongly with the layup of the upper sublaminate as well as the delamination depth. Therefore, with the aid of a parametric study, 84 generalized coordinates corresponding to $M^u = 8$, $N^u = 3$, $M^v = N^v = 3$, $M_1^w = 4$, $M_2^w = N^w = 2$, $O^w = 1$ (cf. Eq. (18.3)) have been determined to provide satisfac-

tory results, where certain configurations such as unidirectional layups and deeper delaminations (within the thin-film range) may only require 10 generalized coordinates.

18.3 Energy Formalism

18.3.1 Total potential energy principle

Owing to the description of the given problem in cylindrical coordinates, the well-known in-plane (A_{IJ}), coupling (B_{IJ}) and bending (D_{IJ}) stiffness matrices comprised within the Classical Laminate Theory ($\{I,J\}=\{1,2,6\}$) are rewritten employing the coordinate transformation illustrated in Fig. 18.2 (from the local fibre coordinate system $(\boldsymbol{e_1},\boldsymbol{e_2},\boldsymbol{e_3})$ to the cylindrical coordinate system $(\boldsymbol{e_r},\boldsymbol{e_\varphi},\boldsymbol{e_z})$).

With the assumption of plane stress, the reduced transformed stiffness matrix $[\bar{Q}]$ can be expressed in terms of the reduced stiffness matrix $[Q]$ of the respective unidirectional layers (assumed to be transversally isotropic) of the laminate, the fibre orientation angle θ and the angle φ, thus

$$[\bar{Q}](\varphi) = [K][Q][K]^{-\mathrm{T}}, \text{ with} \tag{18.5}$$

$$[K] = \begin{bmatrix} \cos^2\omega & \sin^2\omega & 2\sin\omega\cos\omega \\ \sin^2\omega & \cos^2\omega & -2\sin\omega\cos\omega \\ -\sin\omega\cos\omega & \sin\omega\cos\omega & \cos^2\omega-\sin^2\omega \end{bmatrix}, \tag{18.6}$$

$$[Q] = \begin{bmatrix} Q_{11} & Q_{12} & 0 \\ Q_{12} & Q_{22} & 0 \\ 0 & 0 & Q_{66} \end{bmatrix}, \text{ and} \tag{18.7}$$

$$\omega = \varphi - \theta. \tag{18.8}$$

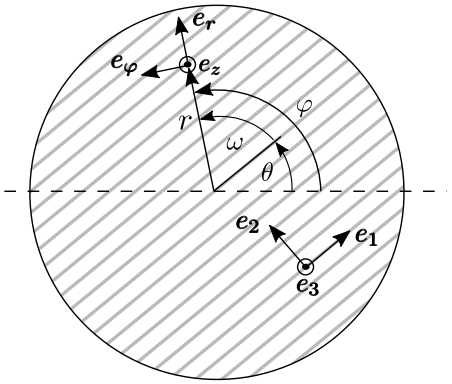

Fig. 18.2 Coordinate transformation from the local fibre coordinate system $(\boldsymbol{e_1},\boldsymbol{e_2},\boldsymbol{e_3})$ to the cylindrical coordinate system $(\boldsymbol{e_r},\boldsymbol{e_\varphi},\boldsymbol{e_z})$.

In order to model the post-buckling response, non-linear strains associated with the out-of-plane displacement (i.e. VON KÁRMÁN strains, see Reddy, 2004) are considered in the modelling approach, thus

$$\begin{aligned}\begin{pmatrix}\varepsilon_{rr}\\ \varepsilon_{\varphi\varphi}\\ 2\varepsilon_{r\varphi}\end{pmatrix} &= \begin{pmatrix}\varepsilon_1\\ \varepsilon_2\\ \varepsilon_6\end{pmatrix} = \left\{\varepsilon^0\right\} + z\left\{\kappa\right\}\\ &= \begin{pmatrix}\dfrac{\partial u}{\partial r} + \dfrac{1}{2}\left(\dfrac{\partial w}{\partial r}\right)^2\\ \dfrac{1}{r}\dfrac{\partial v}{\partial \varphi} + \dfrac{u}{r} + \dfrac{1}{2}\left(\dfrac{1}{r}\dfrac{\partial w}{\partial \varphi}\right)^2\\ \dfrac{1}{r}\dfrac{\partial u}{\partial \varphi} + \dfrac{\partial v}{\partial r} - \dfrac{v}{r} + \dfrac{1}{r}\dfrac{\partial w}{\partial \varphi}\dfrac{\partial w}{\partial r}\end{pmatrix} + \begin{pmatrix}-\dfrac{\partial^2 w}{\partial r^2}\\ -\dfrac{1}{r^2}\dfrac{\partial^2 w}{\partial \varphi^2} - \dfrac{1}{r}\dfrac{\partial w}{\partial r}\\ -\dfrac{2}{r}\dfrac{\partial^2 w}{\partial r \partial \varphi} + \dfrac{2}{r^2}\dfrac{\partial w}{\partial \varphi}\end{pmatrix},\end{aligned} \tag{18.9}$$

where $\{\varepsilon^0\}$ and $\{\kappa\}$ are the membrane strains and the curvatures, respectively.

The strain energy W_s is determined by integrating the strain energy density,

$$w_\mathrm{s} = \frac{1}{2}\bar{Q}_{IJ}\varepsilon_I\varepsilon_J, \tag{18.10}$$

over the volume, yielding

$$W_\mathrm{s} = \frac{1}{2}\int_\varphi\int_r \left(\varepsilon_I^0 A_{IJ}\varepsilon_J^0 + 2\varepsilon_I^0 B_{IJ}\kappa_J + \kappa_I D_{IJ}\kappa_J\right) r\,\mathrm{d}r\,\mathrm{d}\varphi, \tag{18.11}$$

where the displacement field defined in Eqs. (18.2) and (18.3) as well as Eq. (18.9) are employed, with $W_\mathrm{s} = W_\mathrm{s}^{\textcircled{1}} + W_\mathrm{s}^{\textcircled{2}} + W_\mathrm{s}^{\textcircled{3}}$. It should be noted that, in Eq. (18.11), the in-plane (A_{IJ}), coupling (B_{IJ}) and bending stiffness (D_{IJ}) matrices depend on the angle φ. Owing to the displacement controlled problem description, the strain energy is the governing functional. Thus, the post-buckling response can be determined by the well-known variational principle

$$\delta W_\mathrm{s}(q_i) = \frac{\partial W_\mathrm{s}}{\partial q_i}\delta q_i = 0 \quad \text{yielding} \quad \frac{\partial W}{\partial q_i} = 0, \tag{18.12}$$

where the set of non-linear algebraic equations is solved using the NEWTON–RAPHSON method. Owing to the presence of the delamination, an initial imperfection in the form of a small out-of-plane displacement of the upper sublaminate (amplitude of $t/1000$) is commonly assumed modelling delamination buckling (Sheinman et al, 1998). The energy contributions associated with the imperfection are deducted from Eq. (18.11) (cf. Köllner, 2017). The strain energy (Eq. (18.11)) as well as the equilibrium equations (18.12) are determined analytically.

18.3.2 Energy Release Rate

With the aid of the equilibrium solution $q_i(\varepsilon_0)$ obtained from Eq. (18.12), the energy release rate G for delamination growth can be calculated as (cf. Fig. 18.1):

$$G = -\frac{\partial W_\mathrm{s}}{\partial A_\mathrm{del}} \quad \text{with} \quad A_\mathrm{del} = 2 \int_{\varphi_\mathrm{G}-\varphi_0}^{\varphi_\mathrm{G}-\varphi_0+\pi} \int_0^{\Gamma} r \mathrm{d}r \, \mathrm{d}\varphi = R\pi + \frac{1}{4} k \varphi_0 \left(8R + 3k\right). \tag{18.13}$$

Eq. (18.13) can be rewritten, since the onset of delamination growth is determined by a change of the amplitude k of the newly generated delamination area for a certain span φ_0, thus

$$G(\varphi_\mathrm{G}, \varphi_0) = -\frac{1}{\frac{\partial A_\mathrm{del}}{\partial k}} \frac{\partial W_\mathrm{s}}{\partial k}\bigg|_{k=0}. \tag{18.14}$$

Equation (18.14) has to be evaluated for all possible φ_0 (span of delamination growth), i.e. $0 \leq \varphi_0 \leq \pi/2$. Maximizing Eq. (18.14) with respect to φ_0 yields the energy release rate along the boundary of the delamination (φ_G):

$$G(\varphi_\mathrm{G}) = \max_{\varphi_0 \in \left(0, \frac{\pi}{2}\right)} \left(-\frac{1}{\frac{\partial A_\mathrm{del}}{\partial k}} \frac{\partial W_\mathrm{s}}{\partial k}\bigg|_{k=0} \right). \tag{18.15}$$

Even though the calculation of the energy release rate along the boundary of embedded delaminations constitutes a significant advancement in analytical modelling approaches, it should be noted that Eq. (18.15) provides the total amount of the energy release rate. Particularly for embedded delaminations, delamination growth is governed by mode mixture, which is not considered in Eq. (18.15). Therefore, mode mixture is determined by evaluating the force and moment resultants along the boundary of the delamination in conjunction with employing the crack-tip element analysis as described in Schapery and Davidson (1990). Such a crack-tip element, adjusted for the given problem of thin-film delaminations, is illustrated in Fig. 18.3.

In Fig. 18.3, a one-dimensional representation of the crack-tip element is shown. The thin-film assumption is enforced by the supports added to the bottom of the plate. Following Davidson et al (2000, 1995), the lengths d and e as well as the width of the element (annulus) are small enough such that geometric nonlinearities are negligible as well as force and moment resultants remain uniform within the element. As done in Davidson et al (1995), the force and moment resultants $n_{\varphi\varphi}$ and $m_{\varphi\varphi}$ are omitted assuming that they do not affect the crack-tip element (state of plane strain in the width direction of the element). Moreover, it has been shown (e.g. Nilsson et al, 2001) that Mode III remains negligible for the delaminations studied, thus the shear components $n_{r\varphi}$ and $m_{r\varphi}$ are subsequently also omitted.

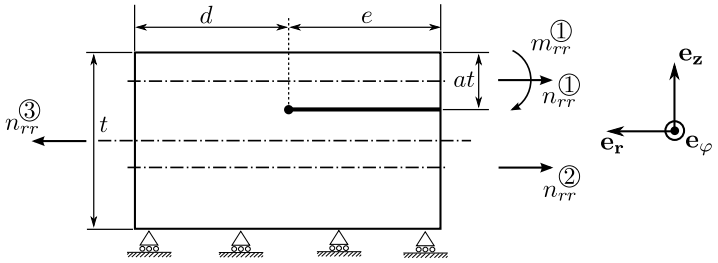

Fig. 18.3 Crack-tip element for the circular composite plate with a thin-film delamination.

With the aid of a free body diagram of the upper sublaminate illustrated in Fig. 18.4, the crack-tip force n_c and moment m_c can be determined:

$$n_\mathrm{c} = -n_{rr}^{\textcircled{1}} + \tilde{n}_{rr}^{\textcircled{3}}, \tag{18.16}$$

$$m_\mathrm{c} = -m_{rr}^{\textcircled{1}} + n_\mathrm{c}\left(\frac{at}{2}\right), \tag{18.17}$$

with $\tilde{n}_{rr}^{\textcircled{3}} = \varepsilon_0\left(A_{11}^{\textcircled{1}} + A_{12}^{\textcircled{1}}\right)$.

The energy release rate G employing the crack-tip forces and resultants as well as the concept of virtual crack closure (Krueger, 2004) can be calculated as

$$G = \frac{1}{2d}\left(n_\mathrm{c}\Delta u + m_\mathrm{c}\Delta\beta\right), \tag{18.18}$$

where $\Delta u = u^{\textcircled{1}} - u^{\textcircled{2}}$ and $\Delta\beta = \beta^{\textcircled{1}}$ are the differences in the displacement of the crack surfaces in the radial direction and in the rotation around the φ-axis respectively, i.e.

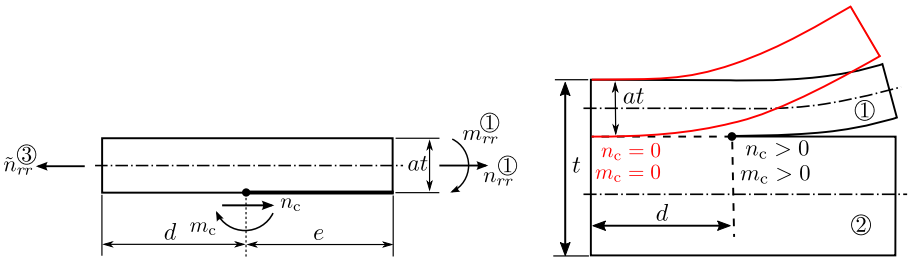

Fig. 18.4 Free-body diagram of the upper sublaminate.

$$
\begin{aligned}
u^{\textcircled{1}} &= d\left(\varepsilon^0_{rr} - \kappa_{rr}\tfrac{at}{2}\right)^{\textcircled{1}}, \\
u^{\textcircled{2}} &= d\,\varepsilon^{0\textcircled{2}}_{rr}, \\
\beta^{\textcircled{1}} &= d\,\kappa^{\textcircled{1}}_{rr}.
\end{aligned}
\tag{18.19}
$$

The parameters Δu and $\Delta\beta$ can also be expressed by the inverted constitutive relation using the crack tip force n_c and moment m_c in conjunction with the compliances (Schapery and Davidson, 1990),

$$
\begin{bmatrix} a_{11} & b_{11} \\ b_{11} & d_{11} \end{bmatrix}^{\textcircled{i}} = \left(\begin{bmatrix} A_{11} & B_{11} \\ B_{11} & D_{11} \end{bmatrix}^{\textcircled{i}} \right)^{-1}, \tag{18.20}
$$

yielding

$$
\begin{aligned}
\Delta u/d &= \left(a^{\textcircled{1}}_{11} + a^{\textcircled{2}}_{11} - b^{\textcircled{1}}_{11} at + d^{\textcircled{1}}_{11} \left(\tfrac{at}{2}\right)^2 \right) n_\mathrm{c} + \left(b^{\textcircled{1}}_{11} - d^{\textcircled{1}}_{11} \tfrac{at}{2} \right) m_\mathrm{c} \\
&= c_{11}\, n_\mathrm{c} + c_{12}\, m_\mathrm{c}, \\
\Delta\beta/d &= \left(b^{\textcircled{1}}_{11} - d^{\textcircled{1}}_{11} \tfrac{at}{2} \right) n_\mathrm{c} + d^{\textcircled{1}}_{11}\, m_\mathrm{c} \\
&= c_{12}\, n_\mathrm{c} + c_{22}\, m_\mathrm{c}\,.
\end{aligned}
\tag{18.21}
$$

With the parameters c_{11}, c_{12} and c_{22} given by Eq. (18.21), the mode mixture between mode I and mode II can be calculated by determining the phase angle $\Psi = \tan^{-1}\sqrt{G_\mathrm{II}/G_\mathrm{I}}$, i.e.

$$
\Psi = \tan^{-1}\left(\frac{\sqrt{c_{11}} n_\mathrm{c} \cos(\Omega) + \sqrt{c_{22}} m_\mathrm{c} \sin(\Omega + \Gamma)}{-\sqrt{c_{11}} n_\mathrm{c} \sin(\Omega) + \sqrt{c_{22}} m_\mathrm{c} \cos(\Omega + \Gamma)} \right), \tag{18.22}
$$

as given in Davidson et al (2000), where $\Gamma = \sin^{-1}(c_{12}(c_{11}c_{22})^{-1/2})$ and Ω is the mode-mix parameter. Note that employing the Classical Laminate Theory, the parameter Ω cannot be determined analytically for thin-film delaminated multilayered plates; experimental (Davidson et al, 2000) or numerical studies (Schapery and Davidson, 1990) are required. In the current work, Ω is determined with the aid of a finite element simulation (cf. Table 18.1) and remains constant for thin-film delaminations (cf. Davidson et al, 2000).

In order to determine the critical energy release rate G_c, Eq. (18.22) is used in a crack growth criterion provided by Hutchinson and Suo (1992), i.e.

$$
G_\mathrm{c} = G_\mathrm{I}\left(1 + \tan^2\left((1-\lambda)\,\Psi\right)\right), \tag{18.23}
$$

with

$$
\lambda = 1 - \frac{2}{\pi}\tan^{-1}\left(\frac{G^\mathrm{II}_\mathrm{c} - G^\mathrm{I1}_\mathrm{c}}{G^\mathrm{I}_\mathrm{c}}\right),
$$

where G_c^I and G_c^{II} are the critical energy release rates for mode I and II respectively.

18.4 Results

The capabilities of the modelling approach are presented in two ways. First, the post-buckling behaviour of a unidirectional laminate with varying delamination depth is studied (Fig. 18.5). Second, the effect of the layup (i.e. angle orientation) on the behaviour of the energy release rate and thus the onset of delamination growth is analysed (Fig. 18.6). A multi-layered composite plate made of 40 CFRP plies is investigated. The material parameters and the dimensions of the plate are provided in Table 18.1. The results obtained are compared with FE simulations performed in Abaqus using SR4 elements.

Table 18.1 Dimensions and material parameters of the circular plate.

E_{11}	137.90 GPa	G_c^I	0.19 N/mm
E_{22}	8.98 GPa	G_c^{II}	0.63 N/mm
G_{12}	7.20 GPa	R	5 mm
ν_{12}	0.3	t	3.556 mm
[a] ν_{23}	0.5	t_{ply}	0.0889 mm
[a] R^*	50 mm	Ω	58°

[a] parameters used for FEM only.

In Fig. 18.5, the post-buckling response of a circular plate with a unidirectional ($[0^\circ_{40}]$) layup and a circular delamination ($R = 5$ mm) for three different delamination depths ($a = \{1/40, 2/40, 3/40\}$) is shown. The post-buckling behaviour is analysed in terms of applied compressive strain against midpoint deflection (top in Fig. 18.5) and compressive force acting on the upper sublaminate against the end-shortening of the plate (bottom in Fig.18.5). Normalization is performed against the buckling load and strain of a respective intact plate with the radius R^*. The midpoint deflection is normalized against the total thickness of the plate t. As expected, Fig. 18.5 shows that with larger delamination depths (a) the buckling load increases and the midpoint deflection during the post-buckling response decreases. This behaviour is verified by the FEM showing very good agreement with the analytical modelling approach. The onset of delamination growth is visualized in Fig. 18.5 by diamond symbols; filled diamonds for the current model and non-filled diamonds the for the FEM. Analysing the force against end-shortening behaviour, it can be seen that delamination growth occurs earlier during the post-buckling response with increasing delamination depth. The prediction of the onset of delamination growth is also in very good agreement with the FEM.

The reason for the accurate prediction of delamination growth in Fig. 18.5 is presented in Fig. 18.6 illustrating the out-of-plane displacements of the delaminated region (top row in Fig. 18.6), the behaviour of the energy release rate along the

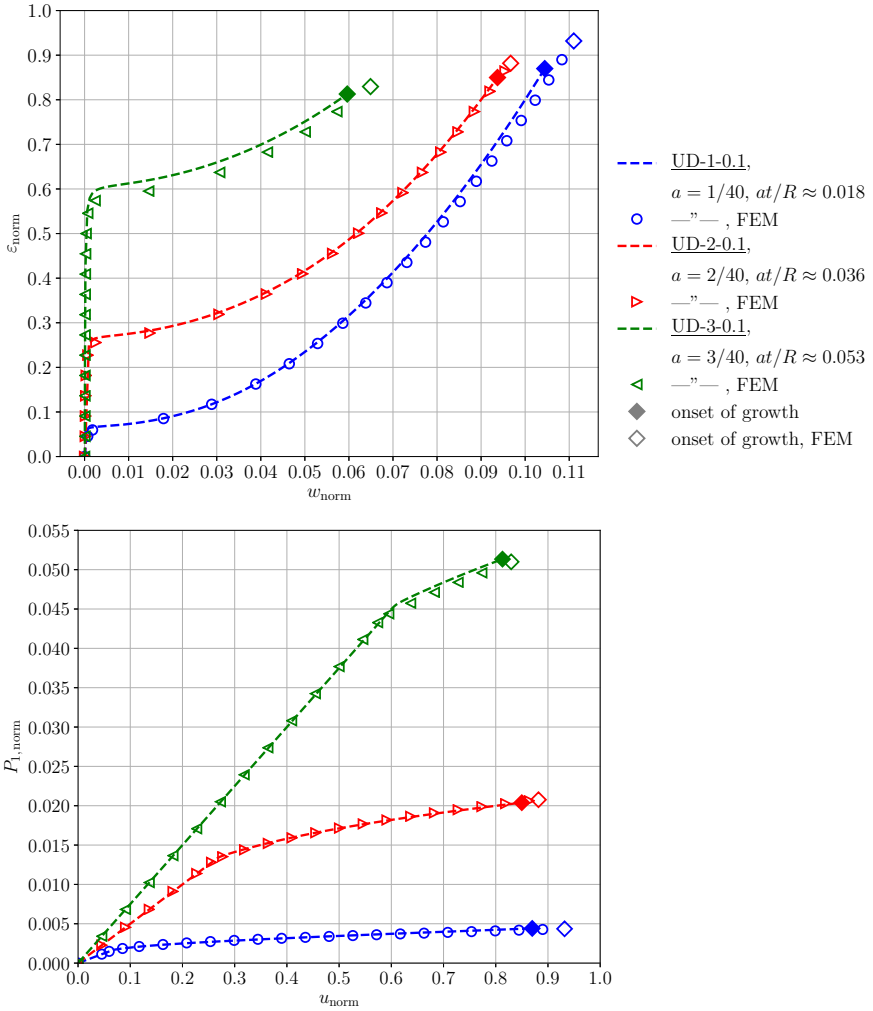

Fig. 18.5 Top: normalized applied compressive strain $\varepsilon_{\mathrm{norm}}$ vs. normalized midpoint deflection w_{norm}; bottom: normalized compressive force P_{norm} vs. normalized end-shortening u_{norm}.

boundary of the delamination (middle row in Fig. 18.6) and the span of delamination growth as well as the phase angle along the boundary (bottom row in Fig. 18.6). A delamination depth of $a = 3/40$ is chosen and three different layups of the upper sublaminate are analysed: **a)** unidirectional $[0_3^\circ]$, **b)** cross-ply $[90^\circ/0^\circ/90^\circ]$ and **c)** an arbitrary angle layup $[45^\circ/0^\circ/45^\circ]$.

Owing to the local geometric representation presented in Sect. 18.2, the behaviour of the energy release rate along the boundary can be analysed (cf. second row of Fig. 18.6). The energy release rate is normalized against the respective criti-

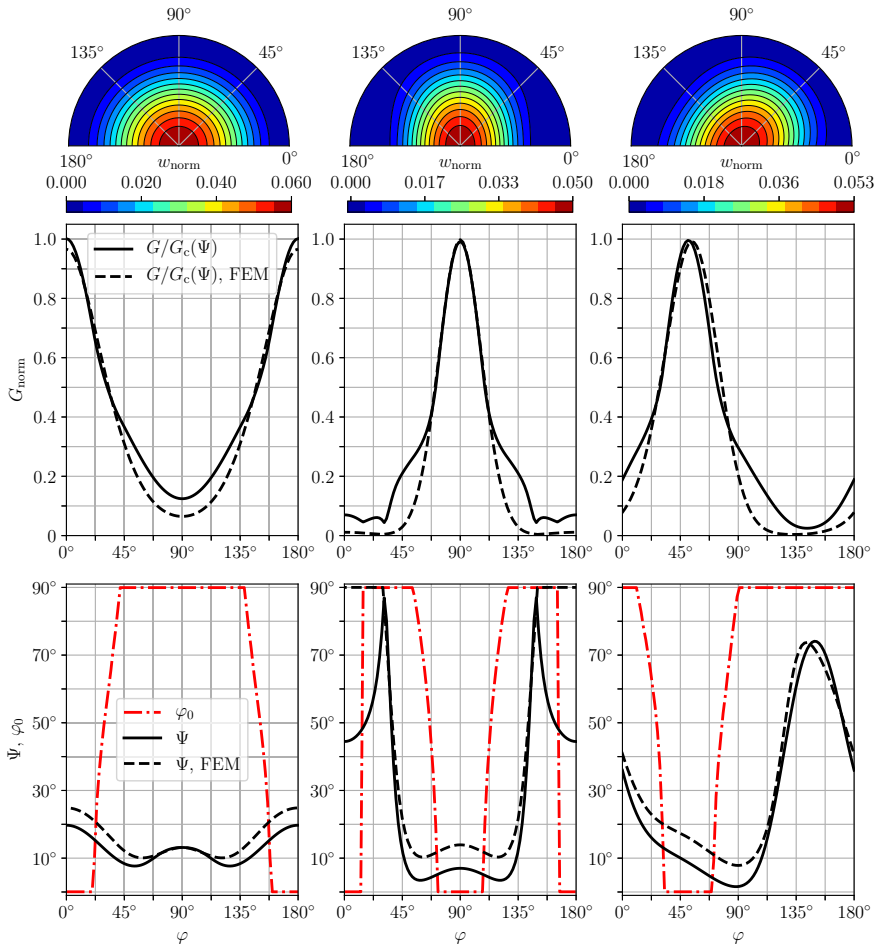

a) layup: $[0^\circ_{40}]$,
$a = 3/40$, $at/R \approx 0.053$,
$\varepsilon^{\mathrm{del}}_{\mathrm{norm}} \approx 0.81$

b) layup: $[(90^\circ/0^\circ)_{20}]$,
$a = 3/40$, $at/R \approx 0.053$,
$\varepsilon^{\mathrm{del}}_{\mathrm{norm}} \approx 0.69$

c) layup: $[(45^\circ/0^\circ)_{20}]$,
$a = 3/40$, $at/R \approx 0.053$,
$\varepsilon^{\mathrm{del}}_{\mathrm{norm}} \approx 0.74$

Fig. 18.6 Normalized out-of-plane displacements of the delaminated region w_{norm} (top), normalized energy release rate G_{norm} along the boundary (middle), span of delamination growth φ_0 and phase angle Ψ along the boundary (bottom); at the onset of growth, $\varepsilon^{\mathrm{del}}_{\mathrm{norm}}$; layups studied: **a)** $[0^\circ_3]$, **b)** $[90^\circ/0^\circ/90^\circ]$, **c)** $[45^\circ/0^\circ/45^\circ]$.

cal energy release rate that depends on the phase angle illustrated in the bottom row of Fig. 18.6. Thus, where $G_{\mathrm{norm}} = 1$ is reached along the boundary, delamination growth occurs. As can be seen in Fig. 18.6, the direction of growth is strongly dependent on the layup of the laminate, where growth for the $[0^\circ_3]$ layup is initiated in

the 0° direction, for $[90^\circ/0^\circ/90^\circ]$ in the 90° direction and for $[45^\circ/0^\circ/45^\circ]$ growth is shifted to approximately 51°.

The normalized applied strain causing delamination growth ($\varepsilon^{\mathrm{del}}_{\mathrm{norm}}$) is provided at the bottom of Fig. 18.6. The unidirectional layup (a) requires the highest applied strain to cause delamination growth. This is related with the phase angle Ψ at the location of the boundary experiencing growth. In growth direction, the unidirectional layup shows the highest value of the phase angle (20°), whereas the layups $[90^\circ/0^\circ/90^\circ]$ and $[45^\circ/0^\circ/45^\circ]$ indicate angles of approximately 7° and 9°, respectively. Larger phase angles, representing larger mode II contributions, increase the critical energy release rate and therefore larger levels of load input are required to reach the respective critical value. The FEM shows qualitatively the same behaviour with small quantitative deviations in the phase angle.

In the bottom row of Fig. 18.6, besides the phase angle, the span of initial delamination growth φ_0 determined by maximizing Eq. (18.14) is plotted along the boundary. As expected, for all cases investigated the initial span of delamination growth tends to zero indicating a localized delamination growth pattern that corresponds well with the FEM where initial delamination growth is given by disbonding of a single node.

18.5 Conclusions

An analytical modelling approach for predicting post-buckling responses and the onset of delamination growth of multi-layered composite plates with a circular delamination has been presented. For the first time, local delamination growth has adequately been modelled by means of a (semi-)analytical approach. This has been enabled by a geometric representation of the newly generated delamination area and a problem description using cylindrical coordinates. Studies employing (semi-)analytical models have hitherto considered delamination growth in a global manner, i.e. growing major and/or minor axis of a circular(elliptical) delamination, which either only applies to certain configurations or yields significant overestimations of the applied load required to cause delamination growth. Thus, with the aid of the modelling approach presented in this work, the capabilities of (semi-)analytical approaches towards a structural stability analysis of delaminated composite structures have been improved significantly.

Despite using cylindrical coordinates as well as the geometric representation of the boundary of the delamination, the total potential energy, the equilibrium equations and the energy release rate have been determined analytically. Post-buckling responses have been determined by only solving once a set of non-linear algebraic equations. As a consequence, efficient parametric studies are enabled which has been demonstrated, in the current work, by studying the effect of varying delamination depths (cf. Fig. 18.5). The adequate prediction of the onset of delamination growth has been enabled by the analysis of the energy release rate along the entire boundary of the delamination, which hitherto could not be done by semi-analytical

modelling approaches. Mode mixture has been considered by employing the crack-tip element analysis, in which the mode mix parameter Ω has been determined with the aid of a finite element simulation. Since Ω mainly depends on the geometry (cf. Davidson et al, 2000), the parameter remains constant for all cases investigated, i.e. for thin-film delaminations, which has been validated by experimental studies in Davidson et al (2000) investigating beam-like structures.

In summary, with the modelling approach developed, a major drawback in semi-analytical models for delamination buckling of embedded delaminations has been overcome, viz. delamination growth can be modelled along the entire boundary. Thus, post-buckling responses of delaminated composite plates considering delamination growth can be determined adequately.

References

Abir MR, Tay TE, Ridga M, Lee HP (2017) Modelling damage growth in composites subjected to impact and compression after impact. Compos Struct 168:13–25

Baker AA, Murray LS (2016) Composite Materials for Aircraft Structures. AIAA Education Series

Bottega WJ, Maewal A (1983) Post-buckled propagation model for compressive fatigue of impact damaged laminates. J Appl Mech 50(1):184–189

Butler R, Rhead AT, Liu W, Kontis N (2012) Compressive strength of delaminated aerospace composites. Phil Trans R Soc Lond A 370:1759–1779

Chai H, Babcock CD (1985) Two-dimensional modelling of compressive failure in delaminated laminates. J Compos Mater 19:67–98

Chai H, Babcock CD, Knauss WG (1981) One dimensional modelling of failure in laminated plates by delamination buckling. Int J Solids Struct 17(11):1069–1083

Chen X, Wu Z, Nie G, Weaver P (2018) Buckling analysis of variable angle tow composite plates with a through-the-width or an embedded rectangular delamination. Int J Solids Struct 138:166–180

Davidson BD, Hurang H, Schapery RA (1995) An analytical crack-tip element for layered elastic structures. J Appl Mech-T ASME 62:294–305

Davidson BD, Gharibian SJ, Yu L (2000) Evaluation of energy release rate-based approaches for predicting delamination growth in laminated composites. Int J Fract 105(4):343–365

Hutchinson JW, Suo Z (1992) Mixed mode cracking in layered materials. Adv Appl Mech 29:63–191

Ipek G, Arman Y, Celik A (2018) The effect of delamination size and location to buckling behavior of composite materials. Composites Part B 155:69–76

Kachanov LM (1976) Separation failure of composite materials. Poly Mech 12(5):812–815

Köllner A (2017) An analytical framework for the structural stability analysis of damageable structures and its application to delaminated composites. Dissertation, Technische Universität Berlin

Köllner A, Völlmecke C (2017a) An analytical framework to extend the general structural stability analysis by considering certain inelastic effects—theory and application to delaminated composites. Compos Struct 170:261–270

Köllner A, Völlmecke C (2017b) Buckling and postbuckling behaviour of delaminated composite struts. Int J Comput Meth Eng Sci Mech 18(1):25–33

Köllner A, Völlmecke C (2018) Post-buckling behaviour and delamination growth characteristics of delaminated composite plates. Compos Struct 203:777–788

Köllner A, Kashtalyan M, Guz I, Völlmecke C (2018) Modelling cracked cross-ply laminates with delamination buckling. Key Eng Mater 774:60–65

Krueger R (2004) Virtual crack closure technique: History, approach, and applications. Appl Mech Rev 57(2):109–143

Nilsson KF, Asp LE, Alpman JE, Nystedt L (2001) Delamination buckling and growth for delaminations at different depths in a slender composite panel. Int J Solids Struct 38:3039–3071

Ouyang T, Sun W, Guan Z, Tan R, Li Z (2018) Experimental study on delamination growth of stiffened composite panels in compression after impact. Compos Struct 206:791–800

Reddy JN (2004) Mechanics of laminated composite plates and shells: theory and analysis. CRC press

Rhead AT, Butler R, Hunt GW (2017) Compressive strength of composite laminates with delamination-induced interaction of panel and sublaminate buckling modes. Compos Struct 171:326–334

Schapery RA, Davidson BD (1990) Prediction of energy release rate for mixed-mode delamination using classical plate theory. Appl Mech Rev 43(5):281–287

Sheinman I, Kardomateas GA, Pelegri AA (1998) Delamination growth during pre- and post-buckling phases of delaminated composite laminates. Int J Solids Struct 35(1-2):19–31

Sun XC, Hallet SR (2018) Failure mechanisms and damage evolution of laminated composites under compression after impact (cai): experimental and numerical study. Composites Part A 104:41–59

Tan W, Falzon BG, Chiu LNS, Price M (2016) Predicting low velocity impact damage and compression-after-impact(cai) behaviour of composite laminates. Composites Part A 71:212–226